Applied Surface Science 430 (2018) 561–570

Contents lists available at ScienceDirect

Applied Surface Science

journal homepage: www.elsevier.com/locate/apsusc

Full Length Article

Facile synthesis of $Bi_2MoO_6/ZnSnO_3$ heterojunction with enhanced visible light photocatalytic degradation of methylene blue

Yue Liu[a,b], Zhao-Hui Yang[a,b,*], Pei-Pei Song[a,b], Rui Xu[a,b], Hui Wang[a,b]

[a] College of Environmental Science and Engineering, Hunan University, Changsha 410082, PR China
[b] Key Laboratory of Environment Biology and Pollution Control, Hunan University, Ministry of Education, Changsha 410082, PR China

ARTICLE INFO

Article history:
Received 14 March 2017
Received in revised form 20 June 2017
Accepted 21 June 2017
Available online 27 June 2017

Keywords:
Composite semiconductors
Visible light photocatalysis
BMZ
Characterization
Superoxide radicals

ABSTRACT

In this paper, visible-light-driven $Bi_2MoO_6/ZnSnO_3$ (BMZ) hybrid photocatalysts were successful fabricated by a combined solvothermal (160 °C, 6 h) and annealing steps (450 °C, 1 h). Systematical characterization methods including X-ray photoelectron spectroscopy (XPS), transmission electron microscope (TEM), X-ray diffraction (XRD), N_2 adsorption-desorption isotherms (BET), photoluminescence (PL) spectroscopy and ultraviolet-visible diffuse reflection spectroscopy (DRS) were implemented to further analyze the obtained hybrids. The photocatalytic properties were investigated against degrading methylene blue (MB) under visible light irradiation. Obviously, BMZ hybrid photocatalysts displayed better photocatalytic performance compared with the bare Bi_2MoO_6 and $ZnSnO_3$. Particularly, the highest photocatalytic activity was obtained by the 5-BMZ composite with the degradation efficiency of approximate 95%, which was up to 1.27 times and 7.31 times higher in comparison with pure Bi_2MoO_6 and $ZnSnO_3$, respectively. The superior photocatalytic performances may be derived from the formation of heterojunction and presence of active species including $^{\bullet}O_2^-$ and h^+. Finally, a possible photocatalytic mechanism for improved photocatalytic activity was proposed.

1. Introduction

Photocatalysis, as one of the most hopeful technologies, has attracted considerable attention in hydrogen evolution and removal of hazardous organic pollutants [1–3]. To date, remarkable efforts have been taken to fabricate novel, high-efficient and environment-friendly photocatalysts embodying Ag-based, Bi-containing, In-containing, Cu-containing and Co-containing [2,4]. However, it is found that the narrow excitation wavelength range and the high recombination rate of photogenerated electrons and holes are two major factors limiting the photocatalytic performance of single-phase photocatalyst [5]. In order to overcome the above-mentioned problems, coupling with other semiconductors to construct the heterojunction has attracted extensive interests [6–9].

Nowadays, Bismuth-based semiconductors exhibit several unique advantages including significant UV and visible photocatalytic property, low or non-toxicity, and high cost-effective, which are significant for their wide application in removal of organic contaminant [10–16]. In particularly, bismuth molybdate (Bi_2MoO_6) draws extensive attention due to its visible light response which lies on its narrow band gap (2.5–2.8 eV) [17–20]. What's more, its layered crystal structure comprised of $[Bi_2O_2]^{2+}$ layers octahedral sandwiched between ${MoO_4}^{2-}$ slabs and morphology have a significant impact on photocatalytic performance [21]. However, the application of the single-phase Bi_2MoO_6 is still limited by its high recombination rate of photogenerated charges, poor adsorption capacity and poor visible light harvesting efficiency [22–29]. To the best of our knowledge, various efforts have been focused on improving the photocatalytic properties of bare Bi_2MoO_6. Among them, integrating Bi_2MoO_6 with others semiconductors to construct heterojunction has been verified to be an effective way to reduce the recombination of electrons-holes pairs [6,30]. A series of Bi_2MoO_6-based composites such as TiO_2/Bi_2MoO_6 [20,31], C_3N_4/Bi_2MoO_6 [32], Ag_2WO_4/Bi_2MoO_6 [33] and $BiOBr/Bi_2MoO_6$ [34] have been developed and presented enhanced photocatalytic activity [23,35]. However, little attention is paid to introduce Zn-based photocatalysts to improve the photocatalytic property of Bi_2MoO_6.

Zinc stannate ($ZnSnO_3$), as an attractive multifunctional material, has been applied in many fields such as gas sensor, photo-electrochemical device and photocatalyst [36,37]. Meanwhile, its facecentered perovskite where each ZnO_6 octahedron

* Corresponding author at: College of Environmental Science and Engineering, Hunan University, Changsha 410082, PR China.
E-mail address: yzh@hnu.edu.cn (Z.-H. Yang).

http://dx.doi.org/10.1016/j.apsusc.2017.06.231
0169-4332/© 2017 Published by Elsevier B.V.

shares a face with SnO_6 octahedron exerts remarkable role in the optical properties [38]. However, compared with other photocatalytic materials, relative less attention is paid to $ZnSnO_3$ in the field of photocatalysis considering its wide band gap [37,39]. Since coupling Fe_3O_4@C with $ZnSnO_3$ has been adopted to resolve its inherent drawback [40], much effort is still needed to further advance the application of $ZnSnO_3$.

Herein, a novel heterojunction photocatalyst BMZ was prepared via a facial solvothermal followed by calcination way. Furthermore, characterization methods including XRD, FTIR, SEM, PL, BET, XPS and DRS were utilized to reveal the formation of heterojunction. It was demonstrated that all the BMZ composites exerted apparently enhanced photocatalytic activity using MB as a model pollutant compared with two single-phase photocatalysts. Also, trapping experiments were conducted to confirm the major active species. The photocatalytic mechanism was elucidated in detail based on the band-structure and results derived from the trapping experiments.

2. Experimental section

2.1. Materials

Zinc acetate dihydrate ($Zn(CH3COO)_2$·2H2O, 99%), sodium molybdate ($Na_2MoO_4·2H_2O$, 99%), polyvinyl pyrrolidone (PVP), sodium hydroxide (NaOH, 98%), ethylene glycol, tin chloride pentahydrate (SnCl4·5H2O, 99%), bismuth nitrate ($Bi(NO_3)_3·5H_2O$, 99%) Methylene blue (MB, $C_{16}H_{18}N_3SCl$), ethylenediamine, and ethanol were obtained from Sinopharm Chemical Reagent Co., Ltd. All other reagents were analytical reagent grade and used without further purification. Deionized water was used from a Hitech-Kflow water purification system.

2.2. Synthesis of BMZ composites

2.2.1. Synthesis of $ZnSn(OH)_6$

In a typical procedure, 5 M $Zn(CH_3COO)_2·2H_2O$ was dissolved in 25 mL deionized water containing 0.5 g PVP under stirring. After the absolute formation of the solution, equal volumes $SnCl_4·5H_2O$ (0.2 M) was dispersed into the abovementioned solution dropwise by dropwise, followed by adding 0.6 M NaOH solution to adjust the solution pH at about 12. After stirring for another 30 min, the obtained solution was placed into a water bath and kept for 6 h at 60 °C. Subsequently, the collected precipitate was cooled and washed thoroughly with ethanol followed by deionized water for several times and dried in an oven at 80 °C for overnight.

2.2.2. Synthesis of BMZ hybrid materials

The BMZ nanocomposite photocatalysts were synthesized through a solvothermal procedure. Briefly, $ZnSn(OH)_6$ were dispersed in 10 mL ethylene glycol with the help of sonification for 0.5 h. Subsequently, 0.6 M $Bi(NO_3)_3·5H_2O$ and 0.3 M $Na_2MoO_4·2H_2O$ were added into the above solution under sonification. After the reaction was completed, the obtained solution was transferred into a 50 mL Teflon-lined autoclave. Then, the autoclave was heated to 160 °C staying for 6 h. When the autoclave was cooled to ambient temperature, the synthetic products were collected via filtrating and washed repeatedly with deionized water and anhydrous ethanol. The target product was collected after dried in a drying oven for 10 h at 80 °C, followed by calcining at 450 °C for 1 h. The mole ratio of Bi_2MoO_6 to $ZnSnO_3$ was set to be 1:1, 3:1, 5:1, 7:1, and the corresponding products were labeled as 1-BMZ, 3-BMZ, 5-BMZ and 7-BMZ, respectively. Both pure $ZnSnO_3$ and Bi_2MoO_6 samples were prepared under the similar process.

2.3. Characterization

The surface element composition analyses were measured with X-ray Photoelectron Spectroscopy (XPS) on a Thermo ESCALAB 250XI spectrometer with Al Kα source. To get the specific surface area of materials, a TRISTAR-3000 surface area analyzer was applied at 77 K via the Brunauer-Emmett-Teller (BET) method. The powder X-ray diffraction (XRD) were implemented via Bruker AXS D8 Advance diffractometer operating with Cu-Kα source (λ = 1.541 Å) to confirm crystallographic properties. The obtained materials were also determined on an IR Prestige-21 spectrometer (Shimadzu, Japan) to record Fourier transform infrared spectrometer (FTIR) spectra. UV–vis spectrophotometer (UV-4100, Shimadza) was used to analyze the optical properties of the as-fabricated materials in the wavelength range of 300–800 nm by the diffuse-reflectance spectroscopy (DRS). The morphologies of as-prepared materials were analyzed by emission scanning electron microscopy (SEM)(JSM-7001F, Japan) and transmission electron microscopy (TEM)(Tecnai G2 F20 S-Twin, USA), while energy-dispersive X-ray spectroscopy (EDS) ascribed to the SEM was used to determine the chemical composition. Perkin-Elmer LS-55 spectrofluorimeter was applied to inspect photoluminescence (PL) spectroscopy.

2.4. Photocatalytic activity measurement

The photocatalytic activity of BMZ composites were evaluated by the ability to decompose methylene blue (MB) solution (10 mg/L) under visible light (λ > 400 nm) irradiation. To obtain the needed irradiation photosource (14 V, 16 A, 15 cm), a 300 W high pressure Xe lamp was provided. Typically, the photcatalytic process was performed as follows: prior to irradiation, 100 mL MB solution as well as 50 mg photocatalyst were mixed in a 250 mL breaker and magnetically stirred under darkness for 60 min to achieve the adsorption equilibrium. Subsequently, the solution was collected followed via centrifuging to move the remained photocatalysts at specific time intervals during the 1 h illumination. In addition, the obtained clear solution was measured at 665 nm via a UV–vis spectroscopy (UV-2250, Shimadzu).

3. Results and discussion

3.1. XRD patterns

Information concerning crystallographic structure of the as-fabricated materials was provided via the XRD patterns. For the pure Bi_2MoO_6, Fig. 1a shows the peaks located at 10.86°, 23.42°, 28.18°, 32.54°, 33.17°, 35.88°, 46.74°, 47.42°, 55.40°, 56.30°, 58.44° and 75.46° can be indexed to the (020), (111), (131), (200), (210), (151), (062), (260), (331), (191), (262) and (420) planes of the orthorhombic phase of Bi_2MoO_6 (PDF card number: 01-072-1524 [41]). Meanwhile, no additional crystal phases are observed, implying no impurities are introduced during the formation process of the material. In the XRD pattern of pure $ZnSnO_3$ (Fig. 1f), two main peaks at 33.14° and 58.38° matched well with the (110) and (300) diffraction planes of cubic $ZnSnO_3$ (PDF card number: 97-005-0404), respectively [38,42]. As for the BMZ composites, all peaks of Bi_2MoO_6 can be clearly noticed, indicating that the crystal structure of Bi_2MoO_6 remains unchanged after the introduction of $ZnSnO_3$ as well as the calcination progress. It should be noted that with the decrease of the Bi_2MoO_6 content in the BMZ composites, the peak intensity of the Bi_2MoO_6 exhibits a relative decline as depicted in Fig. 1b–e. Meanwhile, no obvious peak of $ZnSnO_3$ is discerned in the composites. This may be due to the small dosage amount and poor crystallization of $ZnSnO_3$ in the hybrids. The similar phenomenon has been reported in previous papers [43,44].

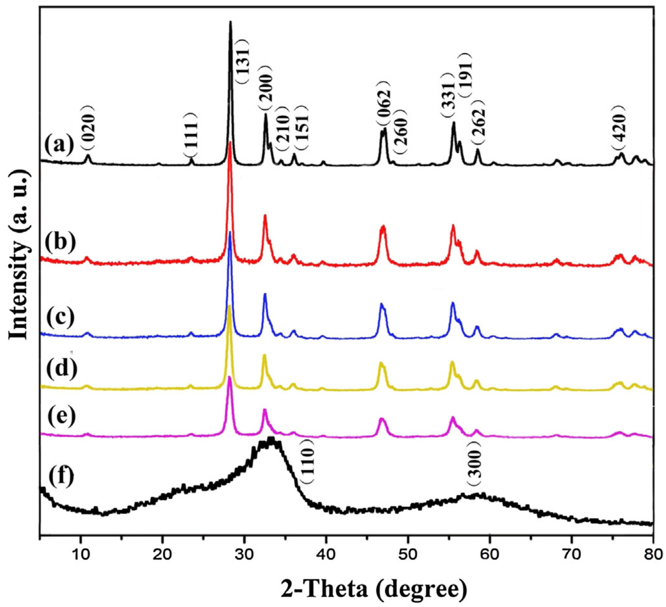

Fig. 1. The XRD patterns of (a) Bi_2MoO_6; (b) 7-BMZ; (c) 5-BMZ; (d) 3-BMZ; (e) 1-BMZ (f) $ZnSnO_3$.

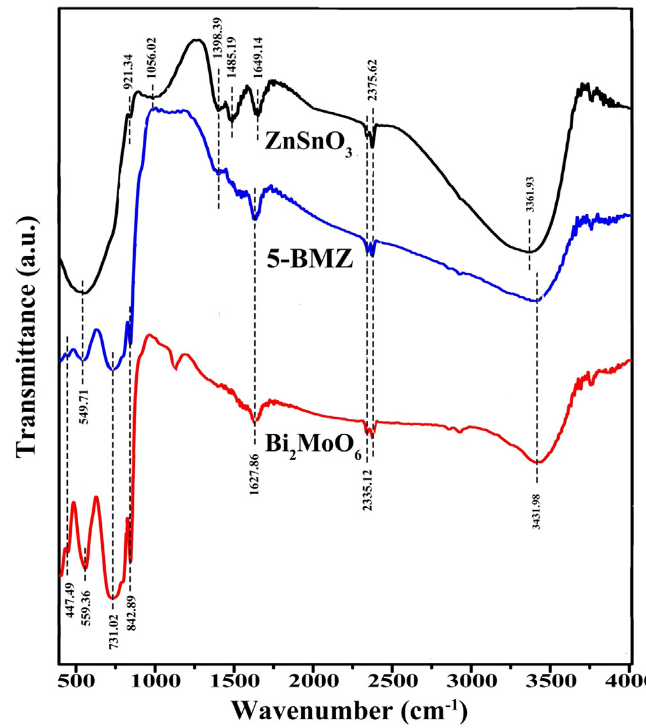

Fig. 2. FT-IR spectra of various photocatalysts: (a) Bi_2MoO_6; (b) 5-BMZ; (c) $ZnSnO_3$.

Additionally, as shown in Fig. S4a, the diffraction peaks at 19.76°, 22.84°, 32.54°, 36.50°, 38.36°, 40.16°, 43.50°, 46.68°, 51.20°, 52.60°, 58.80°, 61.96°, 68.18°, 71.76°, 72.98°, 77.58° can be indexed to the (111), (200), (220), (013), (311), (222), (321), (400), (331), (420), (422), (511), (440), (135), (531), (620) planes of the cubic phase of $ZnSn(OH)_6$ (PDF card number:97-002-767), implying that $ZnSnO_3$ is formed after the calcination step not during the solvothermal treatment. The Fig. S4b also shows that all the peaks of Bi_2MoO_6 after solvothermal reaction match well with the orthorhombic phase of Bi_2MoO_6 (PDF card number: 01-072-1524), which indicates that Bi_2MoO_6 is formed before the calcination step. Herein, the formation situation of Bi_2MoO_6 and $ZnSnO_3$ before calcination step are further confirmed by the XRD pattern of 5-BMZ (Fig. S4c).

3.2. FT-IR characterization

FT-IR analysis was implemented to further reveal the chemical bonds and functional groups of $BiMoO_6$, $ZnSnO_3$ and 5-BMZ composite. In the spectra of as-prepared samples, the peaks centered on 3300–3500 cm^{-1} and 1400–1649 cm^{-1} are contributed by surface-adsorbed water molecules [45,46]. The weak peak located at around 2300 cm^{-1} originates from the asymmetric stretching of carbon dioxide (CO_2) [46]. For pure $BiMoO_6$, the absorption band at approximately 447 cm^{-1} and 559 cm^{-1} are conformed to stretching and deformation vibrations of Bi-O, while Mo-O stretching vibrations are located in 731 cm^{-1} and 843 cm^{-1} as displayed in Fig. 2a [2]. As for the FTIR spectrum of $ZnSnO_3$ (Fig. 2c), the bands at around 550 cm^{-1}, 921 cm^{-1}, 1056 and 1398 cm^{-1} indicate the existence of M-O or M-O-M groups, respectively [42]. In addition, as shown in Fig. 2b, the Bi—O and Mo—O bands attaching to $BiMoO_6$ can be found in the spectrum of 5-BMZ composite. However, peaks of $ZnSnO_3$ are difficult to distinguish in the 5-BMZ hybrid, which may be ascribed to its low content.

3.3. Morphological analysis

In order to reveal the morphology and microstructure of resultant Bi_2MoO_6, $ZnSnO_3$ and 5-BMZ materials, SEM and TEM were conducted. As displayed in Fig. 3a, the pure $BiMoO_6$ reveals aggregated particles composed of many smaller regular 10–30 nm $BiMoO_6$ particles (Fig. 3b) via redouble amplification. What's more, the SEM image of $ZnSnO_3$ (Fig. 3c) exhibits cubic-like shape with wrinkled structure, which is approximately 500–700 nm. The mentioned results concerning morphology were further confirmed by the TEM characterization (Fig. 4a–b). After introducing $ZnSnO_3$, the cubic $ZnSnO_3$ is covered by a large quantity of Bi_2MoO_6 particles with well dispersity (Fig. 3d). This shows that the formation of BMZ composites is identical with the TEM results exhibited in Fig. 4c. In addition, the SEM-EDS mapping of 5-BMZ (Fig. 3e–f) displays that all elements in the composite are uniformly distributed. This further corroborates the successful synthesis of BMZ composites. High-resolution TEM (HRTEM) image of 5-BMZ was introduced to further verify the morphology and structure. Fig. 4d shows the apparent lattice fringes with 0.319 nm, 0.273 nm and 0.196 nm which attributes to (131), (002) and (062) lattice planes of $BiMoO_6$, respectively.

3.4. XPS and BET characterization

The chemical states of various elements in the as-fabricated 5-BMZ hybrids were further investigated by XPS measurements. Fig. 5 depicts the survey spectrum of $BiMoO_6$, $ZnSnO_3$ and 5-BMZ and high-resolution XPS spectra of the Sn, Zn, Bi and Mo regions of 5-BMZ, respectively. Among them, the survey spectrum of 5-BMZ sample (Fig. 5a) reveals that no peaks of other elements excepting Bi, Mo, Sn, Zn, C and O can be observed. Meanwhile, Fig. 5b shows the regional spectrum of Bi 4f,where two predominant peaks at the binding energy of 164.56 eV and 159.28 eV are conformed to Bi $4f_{5/2}$ and Bi $4f_{7/2}$ of 5-BMZ, respectively, implying the existence of Bi^{3+} [32], which shows no obvious change compared with the pure Bi_2MoO_6. Moreover, the binding energy centered at 232.41 eV and 235.55 eV are in accordance with the Mo $3d_{5/2}$ and Mo $3d_{3/2}$ of Mo^{6+} owning to the pure Bi_2MoO_6 in Fig. 5c [28]. After the introduction of $ZnSnO_3$, the double peaks of the hybrid shifts to the 232.53 eV and 235.67 eV, respectively, indicating that $ZnSnO_3$ affects the surface chemical environment of Bi_2MoO_6. In the Zn 2p spectrum (Fig. 5e), peaks at 1044.93 eV and 1021.78 eV for $ZnSnO_3$ are representatively

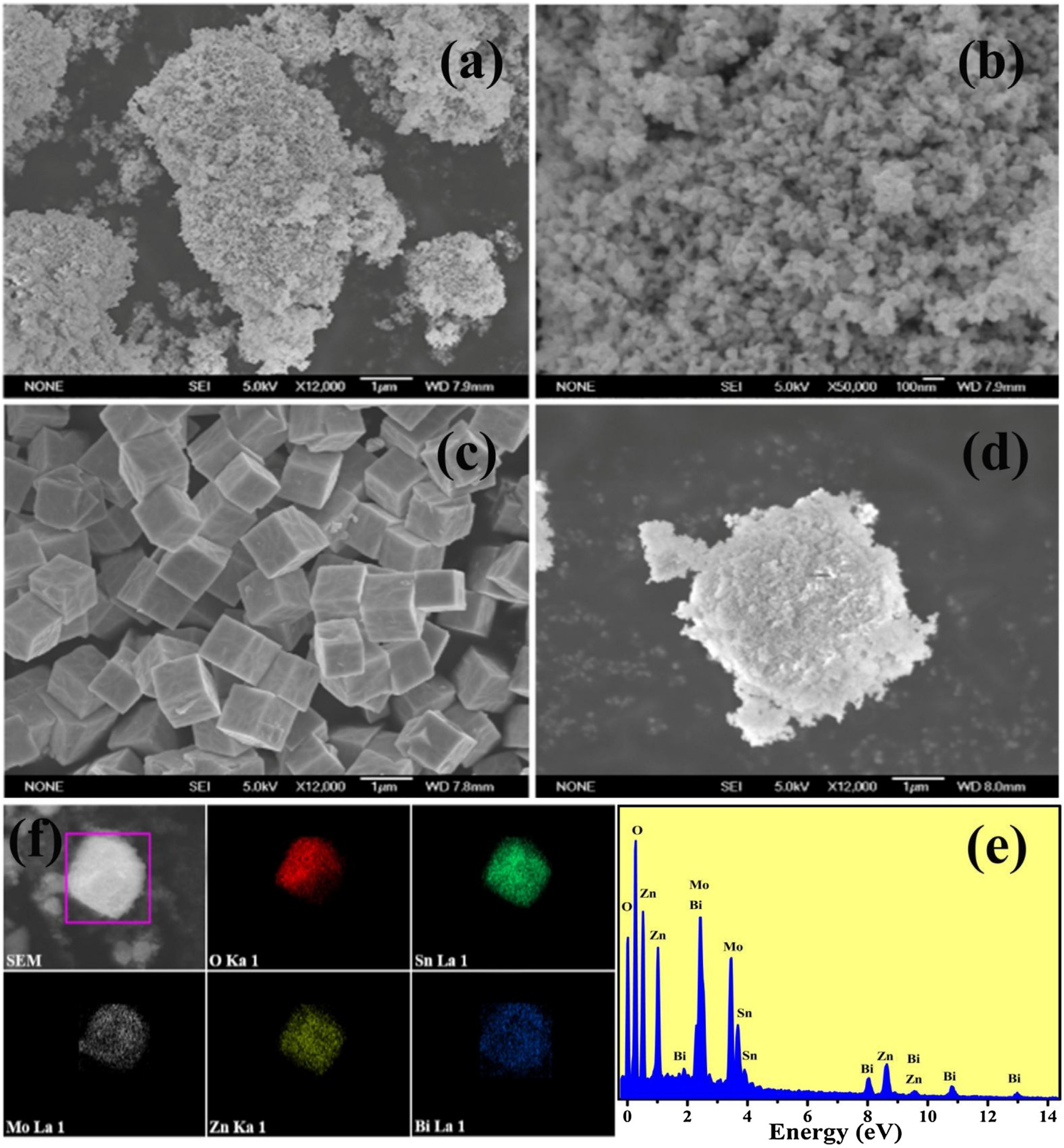

Fig. 3. The SEM images of (a, b) Bi_2MoO_6; (c) $ZnSnO_3$; (d) 5-BMZ; (e) The EDS pattern of 5-BMZ; (f) the SEM-EDS images of O, Sn, Mo, Zn, Bi elements.

conformed to Zn $2p_{1/2}$ and Zn $2p_{3/2}$ of Zn^{2+} [47]. However, compared with that of pure $ZnSnO_3$, the peak positions of Zn $2p_{3/2}$ and Zn $2p_{1/2}$ of 5-BMZ exhibits a positive shift with orders of 0.41 eV and 0.30 eV. As displayed in Fig. 5d, peaks at 494.85 eV and 486.44 eV are assigned to Sn $3d_{5/2}$ and Sn $3d_{3/2}$ of pure $ZnSnO_3$ [48], respectively, which are 0.21 eV and 0.14 eV lower than those of 5-BMZ. Above shifts of Zn 2p and Sn 3d imply that the heterojunction may be formed between $ZnSnO_3$ and Bi_2MoO_6 [49]. In addition, the existence of $ZnSnO_3$ is also depicted via the peaks of Zn 2p and Sn 3d in the composite. Consequently, the successful synthesis of BMZ composite is further corroborated.

To further evaluated the textural properties of as-synthesized $ZnSnO_3$, Bi_2MoO_6 and 5-BMZ samples, N_2 adsorption–desorption measurement was carried out to get the parameters of specific surface area and total pore volume. The corresponding textural properties and curves are depicted in Table 2 and Fig. S1. Obviously, in comparison with bare Bi_2MoO_6 (surface area = 22.545 m^2/g, total pore volume = 0.0833 cm^3/g), and $ZnSnO_3$ (surface area = 66.866 m^2/g, total pore volume = 0.0573 cm^3/g), higher surface area (32.715 m^2/g) and total pore volume (0.1701 cm^3/g) are obtained by the 5-BMZ hybrid, which may be attributed to that the introduction of $ZnSnO_3$ improves slightly the texture of Bi_2MoO_6. Besides, it is found that the measured surface area of $ZnSn(OH)_6$ is 2.75 m^2g^{-1}, which is quite small compared with $ZnSnO_3$. Considering that the $ZnSnO_3$ was obtained after the calcination of $ZnSn(OH)_6$ at 450 °C. During the calcination process,

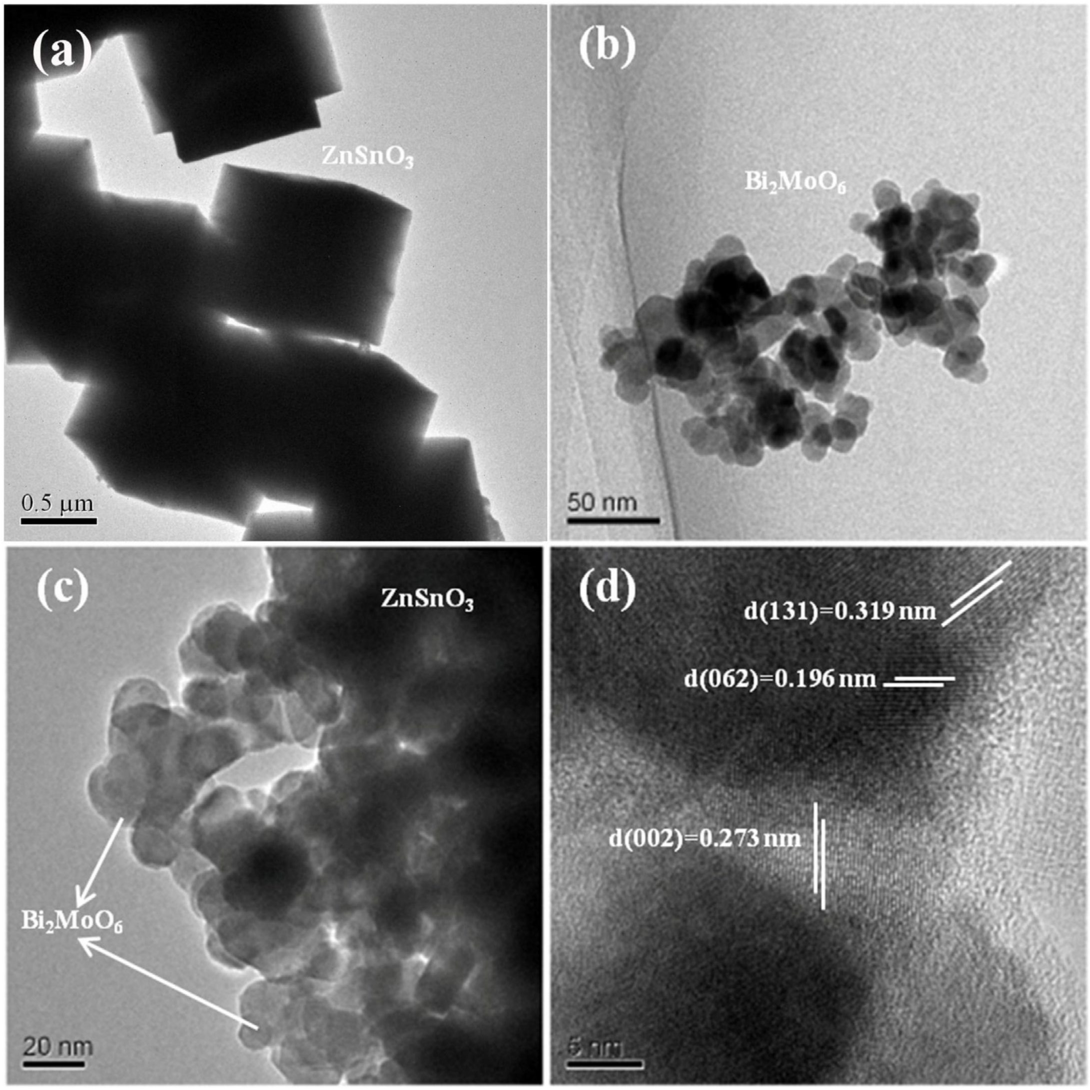

Fig. 4. The TEM images of (a) $ZnSnO_3$; (b) Bi_2MoO_6; (c) 5-BMZ and (d) HRTEM of 5-BMZ.

the $ZnSn(OH)_6$ is turned into $ZnSnO_3$ by the loss of water molecules. Therefore, it is conjectured that the loss of water molecules in the structure of $ZnSn(OH)_6$ during the calcination process result in that the specific surface area of the formed $ZnSnO_3$ is higher than Bi_2MoO_6. Meanwhile, the enhanced surface area and total pore volume of composites can supply more active sites to facilitate electron-hole transport.

3.5. *UV–vis DRS analysis*

Commonly, the optical absorption properties of resultant photocatalysts exert a crucial role during the photocatalytic process. Hence, the UV–vis light photocatalytic properties of bare $ZnSnO_3$, Bi_2MoO_6 and 5-BMZ with different molar ratios were evaluated via the UV–vis diffuse reflectance absorption spectrum over a wavelength range between 200 nm and 800 nm. As illustrated in Fig. 6a, the pure Bi_2MoO_6 exhibits its visible light photocatalytic property with absorption edge around 482 nm, while the wavelength threshold of $ZnSnO_3$ locates at around 389 nm, which only can harvest UV light. Whereas when the $ZnSnO_3$ is introduced in the Bi_2MoO_6 sample, the absorption edges of BMZ hybrids present gradual red shift. For all BMZ composites, the wavelength thresholds are situated about 500 nm. The specific values of BMZ composites are presented in Table 1. The above phenomenon further elucidates that the introduction of $ZnSnO_3$ facilitates the visible light absorption of Bi_2MoO_6, suggesting the interaction between them. The result is consistent with the morphological analysis and XPS analysis.

Table 1
The absorption edge and corresponding k values of the as-prepared BMZ composites.

Samples	Bi_2MoO_6	1-BMZ	3-BMZ
λ (nm)	482	494	500
k (min^{-1})	0.0221	0.0271	0.0379
Samples	5-BMZ	7-BMZ	$ZnSnO_3$
λ (nm)	506	488	389
k (min^{-1})	0.0508	0.0381	0.0021

Table 2
The specific surface area data of Bi_2MoO_6, $ZnSnO_3$, 5-BMZ.

Samples	Bi_2MoO_6	$ZnSnO_3$	5-BMZ
Surface area (m^2 g^{-1})	22.545	66.866	32.715
total pore volume (cm^3/g)	0.0833	0.0573	0.1701

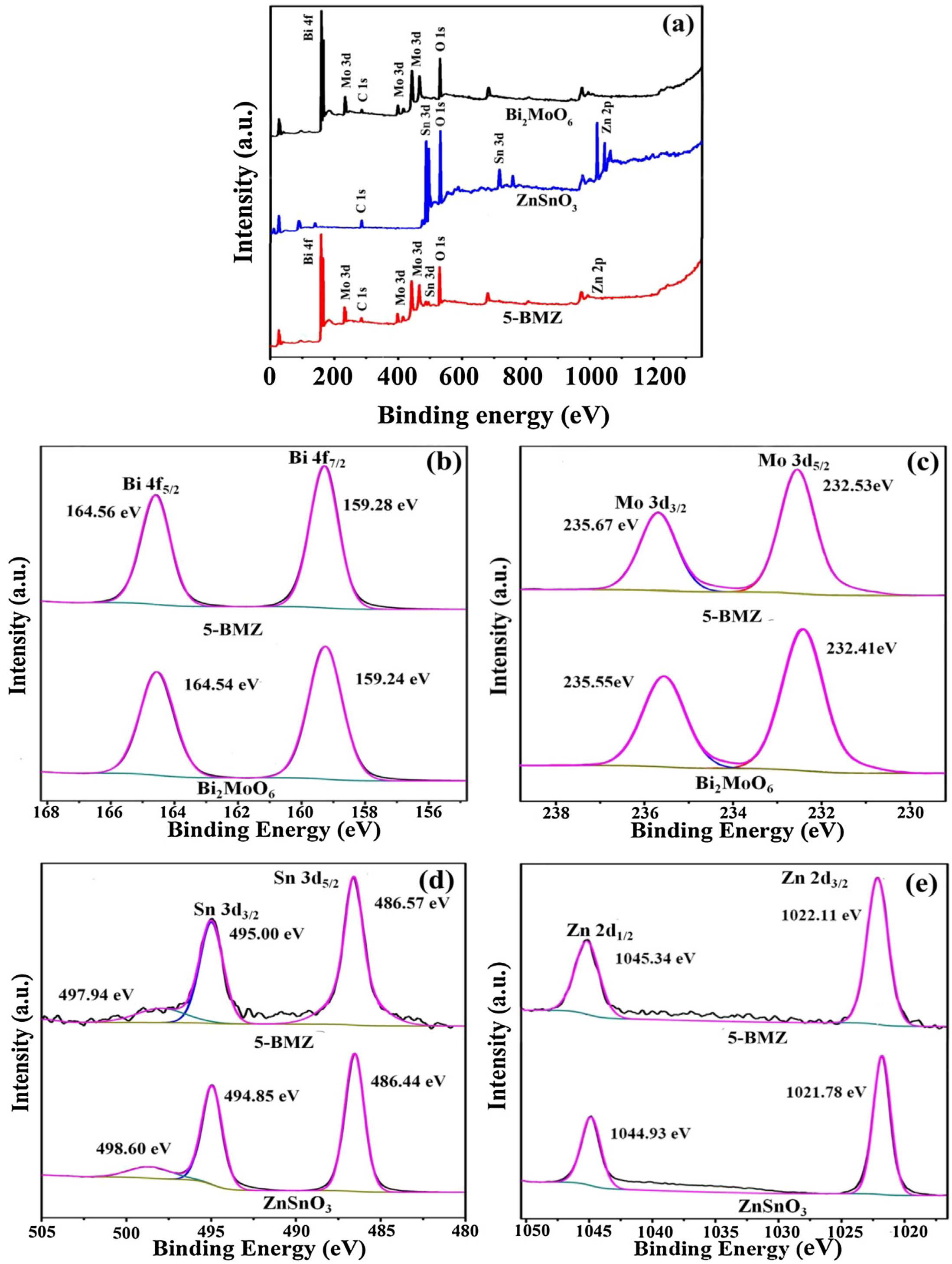

Fig. 5. The XPS spectra of 5-BMZ composite: (a) the survey scans; (b) Bi 4f; (c) Mo 3d; (d) Sn 3d and (e) Zn 2d.

The band gap energy (*Eg*) of Bi_2MoO_6, $ZnSnO_3$ could be verified according to the following Kubelka-Munk function Eq. (1) [50]:

$$(\alpha h\nu)^2 = A(h\nu - Eg) \tag{1}$$

Where α, ν, Eg, h and A are absorption coefficient, light frequency, band gap energy and a constant, respectively. The band gap energies of the $ZnSnO_3$ and Bi_2MoO_6 are also exhibited in Fig. 6b–c.

Furthermore, considering that band edge positions of the photocatalysts exerts an important part on the separation of photoinduced charge carriers. The valence band potential (E_{VB}) and the conduction band potential (E_{CB}) of the bare Bi_2MoO_6 and $ZnSnO_3$ are figured in virtue of the following equations Eqs. (2) and (3) [51]:

$$E_{VB} = X\text{-}Ee + 1/2Eg \tag{2}$$

$$E_{CB} = E_{VB} - Eg \tag{3}$$

Herein, *Ee* is the energy of free electrons in the hydrogen scale (about 4.5 eV) [42]. X is the absolute electronegativity of the semiconductor [52]. By applying the mentioned computing method, the X of $ZnSnO_3$ is 6.06 eV [53], while that of Bi_2MoO_6 is 5.08 eV [54]. Meanwhile, the E_{VB} of the as-synthesized Bi_2MoO_6 and $ZnSnO_3$

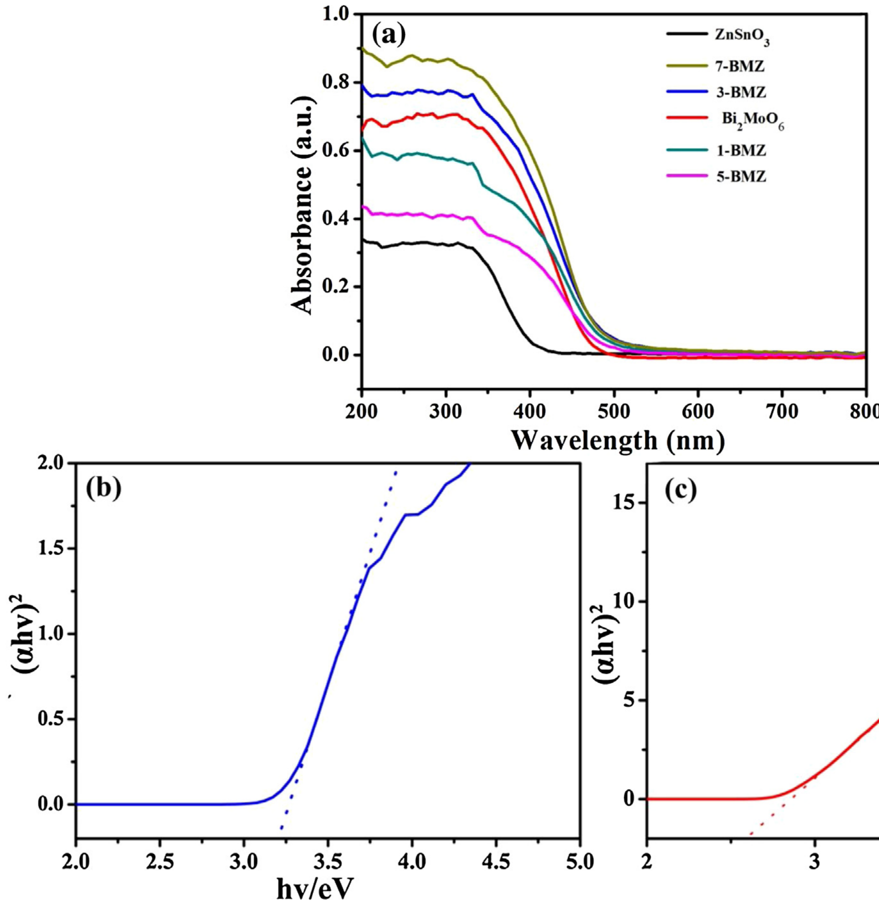

Fig. 6. (a) The UV–vis diffuse reflectance spectra of as-prepared Bi_2MoO_6, $ZnSnO_3$ and BMZ composites; (b) The band gap energy of as-prepared $ZnSnO_3$; (c) The band gap energy of as-prepared Bi_2MoO_6.

samples are 1.87 eV and 3.18 eV, while the E_{CB} are −0.71 eV and −0.06 eV, respectively.

3.6. Photocatalytic activity

To investigate the photocatalytic efficiency of BMZ materials, a representative organic pollutant MB was implemented under visible light irradiation. For comparison, blank tests were carried out at the identical conditions except the absence of either irradiation or photocatalyst. The results (Fig. 7a) demonstrate that the adsorption of MB on the surface of photocatalysts is negligible. As presented in Fig. 7a, compared with the single photocatalytic activities of Bi_2MoO_6 and $ZnSnO_3$, the composites shows markedly higher photocatalytic activities after 1 h irradiation. Interestingly, further observation from Fig. 7a, with the content of the Bi_2MoO_6 in the composite increasing from molar ratio of BMZ 1–7, the photocatalytic activities of BMZ composites increase firstly, and then decrease. Significantly, 5-BMZ exhibits the optimal activity with the degradation rate of nearly 95% after 1 h visible light irradiation while that of Bi_2MoO_6 and $ZnSnO_3$ are around 75% and 12%, respectively. Furthermore, the UV–vis absorption spectra (Fig. S2) of MB over Bi_2MoO_6 and 5-BMZ also present relative decline with the irradiation time increasing, which is fit well with the results obtained from photocatalytic activities test.

What's more, the photocatalytic oxidation process was also investigated via the pseudo first-order kinetic model as shown in Fig. 7b and Table 1. It is obvious that the photocatalytic degradation data fits well with pseudo-first-order model, which is denoted as follows Eq. (4) [55]:

$$\ln(C_t/C_0) = -kt \quad (4)$$

Where k, C_t and C_0 are the apparent rate constant (min^{-1}), the MB concentrations at reaction time t and 0, respectively. In Fig. 7b, the apparent rate constant values for $ZnSnO_3$ and Bi_2MoO_6 are 0.0021 min^{-1} and 0.0221 min^{-1}, respectively. As for the BMZ hybrid materials, a similar variation trend (Fig. 7a) illustrates that the removal rate constant increases firstly followed by decreasing with the increasing content of Bi_2MoO_6. The highest k value is 0.0508 min^{-1} obtained by 5-BMZ, which is up to 24.19 times and 2.29 times compared with $ZnSnO_3$ and Bi_2MoO_6, respectively. Based on the results, the heterojunction may be constructed between $ZnSnO_3$ and Bi_2MoO_6, which results in the enhanced photocatalytic performance.

3.7. PL spectra

The photoluminescence (PL) measurement was applied to elucidate the separation capacity of photoexcited charge carriers. Commonly, the lower fluorescence intensity means the higher separation efficiency of photoexcited e^--h^+ pairs and vice versa. Fig. 8 depicted that the strong emission peak of Bi_2MoO_6 is detected at appropriately 435 nm when excited at 298 nm. For pure $ZnSnO_3$, the emission intensity was much higher than that of pure Bi_2MoO_6 at similar emission position. It should be noted that 5-BMZ displays the lowest PL intensity compared with pure Bi_2MoO_6 and $ZnSnO_3$. This distinctly corroborates the recombination rate of

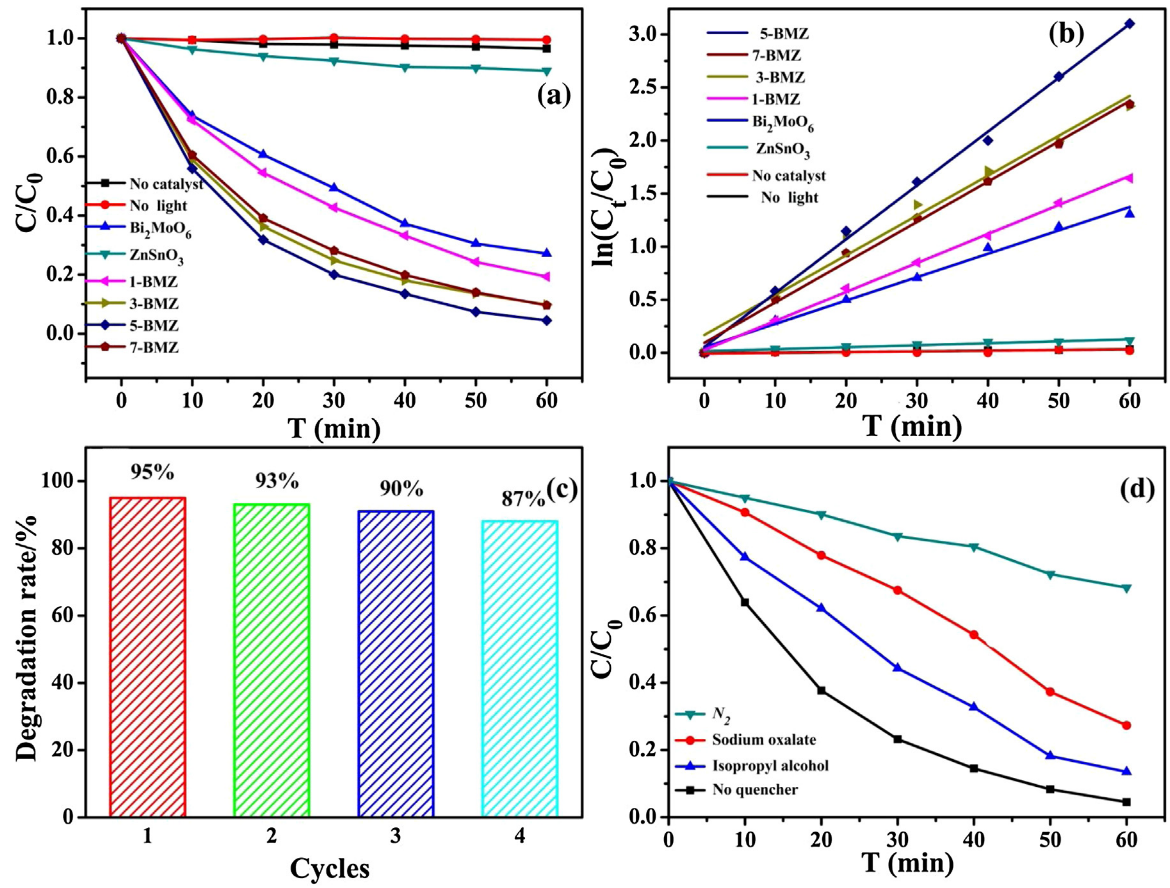

Fig. 7. (a) The MB degradation over no light, no catalyst, Bi_2MoO_6, $ZnSnO_3$ and BMZ composites photocatalysts with different molar ratios; (b) The first-order kinetics plot for the photodegradation of MB; (c) The recycling tests of 5-BMZ composite photocatalyst; (d) The effect of different reactive species scavengers on the photodegradation of MB by 5-BMZ under visual light irradiation.

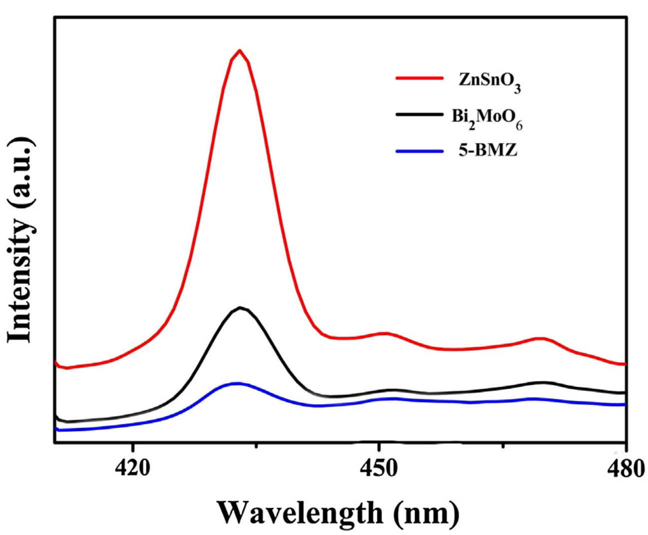

Fig. 8. Photoluminescence (PL) spectra of $ZnSnO_3$, Bi_2MoO_6, 5-BMZ.

photoexcited e^--h^+ pairs is suppressed in the hybrid materials, which is consistent with the results of photocatalytic activity test.

3.8. Photocatalytic mechanism

It is known that reactive species generated in the photocatalysis process make great contributions to the degradation of dye. To deeply reveal the photocatalytic mechanism of BMZ hybrids, scavengers for holes and free radicals were applied in control experiments. Among them, isopropyl alcohol and sodium oxalate were used for hydroxyl radicals ($^•OH$) and holes (h^+) scavengers [11,56]. To reveal the effect of superoxide radicals ($^•O_2^-$), control experiments were carried out under N_2-saturated atmosphere [11,56,57]. The results displayed in Fig. 7d states that the degradation efficiency is markedly suppressed under N_2-saturated condition. The degradation rate reduces from 95% in the absence of any reactive species scavengers to 41%. Considering that the reaction system might not exist $^•O_2^-$ under N_2-saturated condition, Superoxide radical ($^•O_2^-$) might exert a leading part in the MB degradation. Besides, after the addition of sodium oxalate, the degradation rate also presents an obvious decline with ranging from 95% to 72%, which confirms the indispensable influence of h^+. However, when isopropyl alcohol is introduced into the reaction system, a relatively poor suppression about 8% is provoked compared with N_2, which is close to the result without any radical scavengers, suggesting that the influence of $^•OH$ can be negligible. Herein, $^•O_2^-$ and h^+ are the dominant reactive species which can efficiently facilitate the MB degradation under visible light irradiation.

According to the above mentioned results, a reasonable enhanced mechanism associated with the band-edge potential levels and photogenerated carrier efficient separation is elucidated in Fig. 9. After the visible light irradiation, the Bi_2MoO_6 (*Eg* = 2.57 eV) can be excited easily to produce electrons-holes. However, as for $ZnSnO_3$, it is difficult to generate the charge carriers due to its broader band gap (*Eg* = 3.24 eV), which results in a weaker photocatalytic property. Based on the matching CB levels, the flow of photo-excited electrons from CB of Bi_2MoO_6 (-0.71 eV vs.NHE)

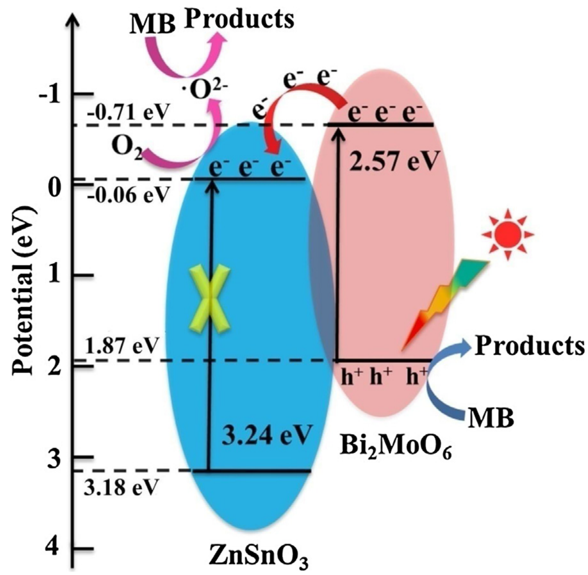

Fig. 9. The photocatalytic degradation mechanism of MB over BMZ composites.

to the CB of $ZnSnO_3$ (-0.06 eV vs.NHE) occurs, leading to the accumulation of electrons in the CB of $ZnSnO_3$. Meanwhile, the holes stay in the VB of Bi_2MoO_6. On the other hand, it means that the CB of $ZnSnO_3$ serves as the sink of photogenerated electrons, which suppresses the rapid recombination of photoinduced electron-hole pairs on the surface of Bi_2MoO_6. The CB level of $ZnSnO_3$ are more negative than the reduction potential of oxygen E_0 ($O_2/{}^\bullet O_2^-$) = (-0.046 eV vs. NHE) [48,58–60], indicating that the molecular oxygen (O_2) can be reduced to superoxide radicals (${}^\bullet O_2^-$) during the transmitting progress of electrons. The superoxide radicals (${}^\bullet O_2^-$) are the primary activity species to decompose MB. Meanwhile, MB molecules can be oxidized via the holes left in VB of Bi_2MoO_6. However, compared with the standard redox potential E_0 (${}^\bullet OH/OH^-$ = +2.38 eV vs. NHE) [61], the VB of Bi_2MoO_6 is not positive enough to generate $^\bullet$OH. This is conformed to the results obtained from trapping experiments. Also, the above process can be clarified as follows:

$$BMZ + h\nu \rightarrow BMZ\ (e^- + h^+) \quad (4)$$

$$Bi_2MoO_6\ (e^- + h^+) \rightarrow ZnSnO_3\ (e^-) + Bi_2MoO_6\ (h^+) \quad (5)$$

$$O_2 + e^- \rightarrow {}^\bullet O_2^- \quad (6)$$

$${}^\bullet O_2^- + MB \rightarrow \text{product} \quad (7)$$

$$h^+ + MB \rightarrow \text{products} \quad (8)$$

3.9. Recyclability

The recyclability experiment of the photocatalysts was evaluated by four consecutive runs considering their practical applications. As displayed in Fig. 7c, the photocatalytic activity of as-fabricated 5-BMZ shows no distinct decline after four continuous experiments. Meanwhile, compared with the recycling ability of Bi_2MoO_6 which approximately reduced 20% after four recycling tests depicted in Fig. S5, the 5-BMZ shows higher recycling ability. The result further verifies the formation of heterojunction between Bi_2MoO_6 and $ZnSnO_3$, replying the positive effect of the composite structure. Besides, there are no obvious changes in the crystal structure between the fresh and recycled 5-BMZ photocatalysts observed from the XRD patterns (Fig. S3). The aboved results suggest that 5-BMZ possesses the photocatalytic stability without photocorrosion. Furthermore, the slight decline might be ascribed to the loss of the photocatalysts for the filtration.

4. Conclusions

In summary, a novel BMZ composites were synthesized via combining a facial solvothermal method and the calcination way. As shown in the work, BMZ composites exhibited the improved photocatalytic activities compared with Bi_2MoO_6 and $ZnSnO_3$. Among them, 5-BMZ presented the highest photocatalytic activity. Additionally, the results from cycle experiments revealed the photocatalysts owned excellent reusability and stability. Based on the tests of radical scavengers, superoxide radicals (${}^\bullet O_2^-$) exerted a dominated role on the photodegradation of MB compared with holes, with the negligible influence caused by $^\bullet$OH. Consequently, the novel composite materials with enhanced photocatalytic activity presented a potential candidate in the settlement of environmental protection issues.

Acknowledgment

This study was sponsored by the National Natural Science Foundation of China (Grants to No. 51578223, 51521006 and 51378189).

Appendix A. Supplementary data

Supplementary data associated with this article can be found, in the online version, at http://dx.doi.org/10.1016/j.apsusc.2017.06.231.

References

[1] L.Q. Ye, J.Y. Liu, Z. Jiang, T.Y. Peng, L. Zan, Facets coupling of BiOBr-g-C_3N_4 composite photocatalyst for enhanced visible-light-driven photocatalytic activity, Appl. Catal. B: Environ. 142–143 (2013) 1–7.
[2] Z.H. Yang, M. Li, M.D. Yu, J. Huang, H.Y. Xu, Y. Zhou, P.P. Song, R. Xu, A novel approach for methylene blue removal by calcium dodecyl sulfate enhanced precipitation and microbial flocculant GA1 flocculation, Chem. Eng. J. 303 (2016) 1–13.
[3] Y.H. Ao, J.L. Xu, P.F. Wang, C. Wang, J. Hou, J. Qian, Y. Li, Bi_2MoO_6 nanosheets deposited TiO_2 nanobelts with spatially branched hierarchical heterostructure for enhanced photocatalytic activity under visible light irradiation, Colloids Surf. A: Physicochem. Eng. Aspects 487 (2015) 66–74.
[4] R.A. He, S.W. Cao, J.G. Yu, Recent advances in morphology control and surface modification of bi-based photocatalysts, Acta Phys. –Chim. Sin. 32 (2016) 2841–2870.
[5] W.J. Shan, Y. Hu, Z.G. Bai, M.M. Zheng, C.H. Wei, In situ preparation of g-C_3N_4/bismuth-based oxide nanocomposites with enhanced photocatalytic activity, Appl. Catal. B: Environ. 188 (2016) 1–12.
[6] H.P. Li, T.X. Hu, R.J. Zhang, J.Q. Liu, W.G. Hou, Preparation of solid-state Z-scheme Bi_2MoO_6/MO (M = Cu $Co_{3/4}$, or Ni) heterojunctions with internal electric field-improved performance in photocatalysis, Appl. Catal. B: Environ. 188 (2016) 313–323.
[7] A.A. Firooz, A.R. Mahjoub, A.A. Khodadadi, M. Movahedi, High photocatalytic activity of Zn_2SnO_4 among various nanostructures of $Zn_{2x}Sn_{1-x}O_2$ prepared by a hydrothermal method, Chem. Eng. J. 165 (2010) 735–739.
[8] H.L. Wang, L.S. Zhang, Z.G. Chen, J.Q. Hu, S.J. Li, Z.H. Wang, J.S. Liu, X.C. Wang, Semiconductor heterojunction photocatalysts: design, construction, and photocatalytic performances, Chem. Soc. Rev. 43 (2014) 5234–5244.
[9] S.G. Kumar, K.S.R.K. Rao, Physics and chemistry of CdTe/CdS thin film heterojunction photovoltaic devices: fundamental and critical aspects, Energy Environ. Sci 7 (2014) 45–102.
[10] S. Jonjana, A. Phuruangrat, T. Thongtem, S. Thongtem, Synthesis, analysis and photocatalysis of AgBr/Bi_2MoO_6 nanocomposites, Mater. Lett. 172 (2016) 11–14.
[11] K.C. Christoforidis, T. Montini, E. Bontempi, S. Zafeiratos, J.J.D. Jaén, P. Fornasiero, Synthesis and photocatalytic application of visible-light active β-Fe_2O_3/g-C_3N_4 hybrid nanocomposites, Appl. Catal. B: Environ. 187 (2016) 171–180.
[12] S.G. Kumar, K.S.R.K. Rao, Tungsten-based nanomaterials (WO_3 & Bi_2WO_6): modifications related to charge carrier transfer mechanisms and photocatalytic applications, Appl. Surf. Sci. 355 (2015) 939–958.
[13] N. Zhang, R. Ciriminna, M. Pagliaro, Y.J. Xu, Nanochemistry-derived Bi_2WO_6 nanostructures: towards production of sustainable chemicals and fuels induced by visible light, Chem. Soc. Rev. 43 (2014) 5276–5287.
[14] L.W. Zhang, Y.F. Zhu, A review of controllable synthesis and enhancement of performances of bismuth tungstate visible-light-driven photocatalysts, Catal. Sci. Technol. 2 (2012) 694–706.
[15] R.A. He, S.W. Cao, P. Zhou, J.G. Yu, Recent advances in visible light Bi-based photocatalysts, Chin. J. Catal. 35 (2014) 989–1007.

[16] D.L. Huang, G.M. Zeng, C.L. Feng, S. Hu, X.Y. Jiang, L. Tang, F.F. Su, Y. Zhang, W. Zeng, H.L. Liu, Degradation of lead-contaminated lignocellulosic waste by phanerochaete chrysosporium and the reduction of lead toxicity, Environ. Sci. Technol. 42 (13) (2008) 4946–4951.
[17] J. Zhao, Q.F. Lu, Q.Y. Wang, Q.S. Ma, α-Fe_2O_3 nanoparticles on Bi_2MoO_6 nanofibers: one-dimensional heterostructures synergistic system with enhanced photocatalytic activity, Superlattices Microstruct. 91 (2016) 148–157.
[18] S. Jonjana, A. Phuruangrat, S. Thongtem, T. Thongtem, Preparation and enhanced photocatalytic performance of $AgCl/Bi_2MoO_6$ heterojunction, Mater. Lett. 179 (2016) 162–165.
[19] Z.X. Cai, F.M. Li, W. Xu, Y.Q. Jiang, F. Luo, Y.R. Wang, X. Chen, Enhanced performance of photoelectrochemical water oxidation using a three-dimensional interconnected nanostructural photoanode via simultaneously harnessing charge transfer and coating with an oxygen evolution catalyst, Nano Energy 26 (2016) 257–266.
[20] H. Li, T.X. Zhang, C. Pan, C.C. Pu, Y. Hu, X.Y. Hu, E.Z. Liu, J. Fan, Self-assembled Bi_2MoO_6/TiO_2 nanofiber heterojunction film with enhanced photocatalytic activities, Appl. Surf. Sci. 391 (2017) 303–310.
[21] Y.Y. Sun, J. Wu, T.J. Ma, P.C. Wang, C.Y. Cui, D. Ma, Synthesis of $C@Bi_2MoO_6$ nanocomposites with enhanced visible light photocatalytic activity, Appl. Surf. Sci. 403 (2017) 141–150.
[22] S. Jonjana, A. Phuruangrat, S. Thongtem, T. Thongtem, Synthesis of AgI/Bi_2MoO_6 heterojunctions and their photoactivity enhancement driven by visible light, Mater. Lett. 175 (2016) 75–78.
[23] T.T. Zheng, J.Y. Xu, Z.J. Zhang, H.B. Zeng, P_3HT/Bi_2MoO_6 heterojunction with enhanced photocatalytic activity, Mater. Lett. 164 (2016) 640–643.
[24] J. Zhao, Z.D. Liu, Q.F. Lu, Electrospun 1D SiO_2 doped Bi_2MoO_6 microbelts for highly efficient photocatalytic applications, Dyes Pigm. 134 (2016) 553–561.
[25] J.L. Lv, K. Dai, J.F. Zhang, L.H. Lu, C.H. Liang, L. Geng, Z.L. Wang, G.Y. Yuan, G.P. Zhu, In situ controllable synthesis of novel surface plasmon resonance-enhanced $Ag_2WO_4/Ag/Bi_2MoO_6$ composite for enhanced and stable visible light photocatalyst, Appl. Surf. Sci. 391 (2017) 507–515.
[26] Y.N. Zhu, J.J. Mu, G.H. Zheng, Z.X. Dai, L.Y. Zhang, Y.Q. Ma, D.W. Zhang, Morphology, photocatalytic and photoelectric properties of Bi_2MoO_6 tuned by preparation method, solvent, and surfactant, Ceram. Int. 42 (2016) 17347–17356.
[27] Q. Liang, M. Zhang, C. Yao, C.H. Liu, S. Xu, Z.Y. Li, High performance visible-light driven photocatalysts of Bi_2MoO_6-g-C_3N_4 with controllable solvothermal fabrication, J. Photochem. Photobiol. A: Chem. 332 (2017) 357–363.
[28] Y. Ma, Y.L. Jia, L.N. Wang, M. Yang, Y.P. Bi, Y.X. Qi, Exfoliated thin Bi_2MoO_6 nanosheets supported on WO_3 electrode for enhanced photoelectrochemical water splitting, Appl. Surf. Sci. 390 (2016) 399–405.
[29] L. Tang, G.M. Zeng, G.L. Shen, Y.P. Li, Y. Zhang, D.L. Huang, Rapid detection of picloram in agricultural field samples using a disposable immunomembrane-based electrochemical sensor, Environ. Sci. Technol. 42 (4) (2008) 1207–1212.
[30] L. Zhang, W.Z. Wang, L. Zhou, M. Shang, S.M. Sun, Fe_3O_4 coupled BiOCl: a highly efficient magnetic photocatalyst, Appl. Catal. B: Environ. 90 (2009) 458–462.
[31] J.L. Li, X.J. Liu, Z. Sun, L.K. Pan, Novel Bi_2MoO_6/TiO_2 heterostructure microspheres for degradation of benzene series compound under visible light irradiation, J. Colloid Interface Sci. 463 (2016) 145–153.
[32] J. Li, Y.C. Yin, E.Z. Liu, Y.N. Ma, J. Wan, J. Fan, X.Y. Hu, In situ growing Bi_2MoO_6 on g-C_3N_4 nanosheets with enhanced photocatalytic hydrogen evolution and disinfection of bacteria under visible light irradiation, J. Hazard. Mater. 321 (2017) 183–192.
[33] S. Jonjana, A. Phuruangrat, S. Thongtem, O. Wiranwetchayan, T. Thongtem, Preparation and characterization of Ag_3VO_4/Bi_2MoO_6 nanocomposites with highly visible-light-induced photocatalytic properties, Mater. Lett. 180 (2016) 93–96.
[34] S.Y. Wang, X.L. Yang, X.H. Zhang, X. Ding, Z.X. Yang, K. Dai, H. Chen, A plate-on-plate sandwiched Z-scheme heterojunction photocatalyst: BiOBr-Bi_2MoO_6 with enhanced photocatalytic performance, Appl. Surf. Sci. 391 (2017) 194–201.
[35] Z.L. Wang, J.L. Lv, K. Dai, L.H. Lu, C.H. Liang, L. Geng, Large scale and facile synthesis of novel Z-scheme Bi_2MoO_6/Ag_3PO_4 composite for enhanced visible light photocatalyst, Mater. Lett. 169 (2016) 250–253.
[36] Q.J. Liu, H. Qin, Z. Jiao, F.S. Liu, Z.T. Liu, First-principles calculations of structural, elastic, and electronic properties of trigonal $ZnSnO_3$ under pressure, Mater. Chem. Phys. 180 (2016) 75–81.
[37] J.R. Huang, X.J. Xu, C.P. Gu, W.Z. Wang, B.Y. Geng, Y.F. Sun, J.H. Liu, Size-controlled synthesis of porous $ZnSnO_3$ cubes and their gas-sensing and photocatalysis properties, Sens. Actuators B: Chem. 171–172 (2012) 572–579.
[38] P. Luo, H.J. Zhang, L. Liu, L. Fang, Y. Wang, Sandwich-like nanostructure of amorphous $ZnSnO_3$ encapsulated in carbon nanosheets for enhanced lithium storage, Electrochim. Acta 219 (2016) 734–741.
[39] M.K. Lo, S.Y. Lee, K.S. Chang, Study of $ZnSnO_3$-nanowire piezophotocatalyst using two-step hydrothermal synthesis, J. Phys. Chem. C 119 (2015) 5218–5224.
[40] D.W. Liang, S.L. Wu, P.P. Wang, Y.Y. Cai, Z.F. Tian, J. Liu, C.H. Liang, Recyclable chestnut-like $Fe_3O_4@C@ZnSnO_3$ core–shell particles for the photocatalytic degradation of 2,5-dichlorophenol, RSC Adv. 4 (2014) 26201–26206.
[41] X.C. Meng, Z.S. Zhang, Pd-doped Bi_2MoO_6 plasmonic photocatalysts with enhanced visible light photocatalytic performance, Appl. Surf. Sci. 392 (2017) 169–180.
[42] S. Aziz, K.G. Bum, Y.J. Yang, B.S. Yang, C.U. Kang, Y.H. Doh, K.H. Choi, H.C. Kim, Fabrication of $ZnSnO_3$ based humidity sensor onto arbitrary substrates by micro-Nano scale transfer printing, Sensor Actuat. A: Phys. 246 (2016) 1–8.
[43] J. Xu, X.J. Cao, Characterization and mechanism of MoS_2/CdS composite photocatalyst used for hydrogen production from water splitting under visible light, Chem. Eng. J. 260 (2015) 642–648.
[44] Q.Z. Wang, G.X. Yun, Y. Bai, N. An, J.H. Lian, H.H. Huang, B.T. Su, Photodegradation of rhodamine B with $MoS_2/Bi_2O_2CO_3$ composites under UV light irradiation, Appl. Surf. Sci. 313 (2014) 537–544.
[45] J.H. Zhao, J. Nan, Z.W. Zhao, N. Li, J. Liu, F.Y. Cui, Energy-efficient fabrication of a novel multivalence Mn_3O_4-MnO_2 heterojunction for dye degradation under visible light irradiation, Appl. Catal. B: Environ. 202 (2017) 509–517.
[46] K.N. Abbas, N. Bidin, Morphological driven photocatalytic activity of ZnO nanostructures, Appl. Surf. Sci. 394 (2017) 498–508.
[47] H.Q. Li, W.S. Hong, Y.M. Cui, Q.F. Jia, S.H. Fan, High photocatalytic activity of C-$ZnSn(OH)_6$ catalysts prepared by hydrothermal method, J. Mol. Catal. A: Chem. 378 (2013) 164–173.
[48] F. Chen, Q. Yang, C.G. Niu, X.M. Li, C. Zhang, J.W. Zhao, Q.X. Xu, Y. Zhong, Y.C. Deng, G.M. Zeng, Enhanced visible light photocatalytic activity and mechanism of $ZnSn(OH)_6$ nanocubes modified with AgI nanoparticles, Catal. Commun. 73 (2016) 1–6.
[49] H.Q. Li, Y.M. Cui, W.S. Hong, B.L. Xu, Enhanced photocatalytic activities of $BiOI/ZnSn(OH)_6$ composites towards the degradation of phenol and photocatalytic H_2 production, Chem. Eng. J. 228 (2013) 1110–1120.
[50] Y.C. Huang, W.J. Fan, B. Long, H.B. Li, F.Y. Zhao, Z.L. Liu, Y.X. Tong, H.B. Ji, Visible light $Bi_2S_3/Bi_2O_3/Bi_2O_2CO_3$ photocatalyst for effective degradation of organic pollutions, Appl. Catal. B: Environ. 185 (2016) 68–76.
[51] R.F. Tang, H.F. Su, Y.W. Sun, X.X. Zhang, L. Li, C.H. Liu, S.Y. Zeng, D.Z. Sun, Enhanced photocatalytic performance in Bi_2WO_6/SnS heterostructures: facile synthesis, influencing factors and mechanism of the photocatalytic process, J. Colloid Interface Sci. 466 (2016) 388–399.
[52] H. Wang, X.Z. Yuan, H. Wang, X.H. Chen, Z.B. Wu, L.B. Jiang, W.P. Xiong, G.M. Zeng, Facile synthesis of Sb_2S_3/ultrathin g-C_3N_4 sheets heterostructures embedded with g-C_3N_4 quantum dots with enhanced NIR-light photocatalytic performance, Appl. Catal. B: Environ. 193 (2016) 36–46.
[53] Y. Xu, M.A.A. Schoonen, The absolute energy positions of conduction and valence bands of selected semiconducting minerals, Am. Mineral. 85 (2000) 543–556.
[54] T. Yan, M. Sun, H.Y. Liu, T.T. Wu, X.J. Liu, Q. Yan, W.G. Xu, B. Du, Fabrication of hierarchical $BiOI/Bi_2MoO_6$ heterojunction for degradation of bisphenol A and dye under visible light irradiation, J. Alloys Compd. 634 (2015) 223–231.
[55] F. Chen, Q. Yang, Y. Zhong, H.X. An, W.J. Zhao, T. Xie, Q.X. Xu, X.M. Li, D.B. Wang, G.M. Zeng, Photo-reduction of bromate in drinking water by metallic Ag and reduced graphene oxide (RGO) jointly modified $BiVO_4$ under visible light irradiation, Water Res. 101 (2016) 555–563.
[56] Z.Z. Wu, X.Z. Yuan, H. Wang, Z.B. Wu, L.B. Jiang, H. Wang, L. Zhang, Z.H. Xiao, X.H. Chen, G.M. Zeng, Facile synthesis of a novel full-spectrum-responsive $Co_{2.6}7S_4$ nanoparticles for UV-, vis- and NIR-driven photocatalysis, Appl. Catal. B: Environ. 202 (2017) 104–111.
[57] L.Q. Jing, Y.G. Xu, S.Q. Huang, M. Xie, M.Q. He, H. Xu, H.M. Li, Q. Zhang, Novel magnetic $CoFe_2O_4/Ag/Ag_3VO_4$ composites: highly efficient visible light photocatalytic and antibacterial activity, Appl. Catal. B: Environ. 199 (2016) 11–22.
[58] K. Xiao, H.W. Huang, N. Tian, Y.H. Zhang, Mixed-calcination synthesis of Bi_2MoO_6/g-C_3N_4 heterojunction with enhanced visible-light-responsive photoreactivity for RhB degradation and photocurrent generation, Mater. Res. Bull. 83 (2016) 172–178.
[59] Y.H. Xiang, P. Ju, Y. Wang, Y. Sun, D. Zhang, J.Q. Yu, Chemical etching preparation of the Bi_2WO_6/BiOI p–n heterojunction with enhanced photocatalytic antifouling activity under visible light irradiation, Chem. Eng. J. 288 (2016) 264–275.
[60] S.G. Kumar, K.S.R.K. Rao, Comparison of modification strategies towards enhanced charge carrier separation and photocatalytic degradation activity of metal oxide semiconductors (TiO_2, WO_3 and ZnO), Appl. Surf. Sci. 391 (2017) 124–148.
[61] H. Wang, X.Z. Yuan, H. Wang, X.H. Chen, Z.B. Wu, L.B. Jiang, W.P. Xiong, Y. Zhang, G.M. Zeng, One-step calcination method for synthesis of mesoporous g-$C_3N_4/NiTiO_3$ heterostructure photocatalyst with improved visible light photoactivity, RSC Adv. 5 (2015) 95643–95648.